energies

MDPI

Article

Study on the Electromagnetic Design and Analysis of Axial Flux Permanent Magnet Synchronous Motors for Electric Vehicles

Jianfei Zhao *, Qingjiang Han, Ying Dai and Minqi Hua

School of Mechatronic Engineering and Automation, Shanghai University, Baoshan District, Shanghai 200444, China

* Correspondence: jfzhao@shu.edu.cn; Tel.: +86-021-6613-0935

Received: 30 July 2019; Accepted: 3 September 2019; Published: 6 September 2019

Abstract: In order to provide a complete solution for designing and analyzing the axial flux permanent magnet synchronous motor (AFPMSM) for electric vehicles, this paper covers the electromagnetic design and multi-physics analysis technology of AFPMSM in depth. Firstly, an electromagnetic evaluation method based on an analytical algorithm for efficient evaluation of AFPMSM was studied. The simulation results were compared with the 3D electromagnetic field simulation results to verify the correctness of the analytical algorithm. Secondly, the stator core was used to open the auxiliary slot to optimize the torque ripple of the AFPMSM, which reduced the torque ripple peak-to-peak value by 2%. From the perspective of ensuring the reliability, safety, and driving comfort of the traction motor in-vehicle working conditions, multi-physics analysis software was used to analyze and check the vibration and noise characteristics and temperature rise of several key operating conditions of the automotive AFPMSM. The analysis results showed that the motor designed in this paper can operate reliably.

Keywords: AFPMSM; analytical algorithm; torque ripple; vibration noise; temperature field analysis

1. Introduction

Drive motors used in new energy vehicles require frequent start-ups and shutdowns, are subject to large accelerations or decelerations, and require high-speed, low-torque mode operation. Compared with radial flux permanent magnet synchronous motors (RFPMSM) [1–4], axial flux permanent magnet synchronous motors (AFPMSM) have the advantages of compact axial structure and high power density, which are suitable for new energy vehicles. As early as 2005, researchers have studied AFPMSMs. Methods of finite-element analysis and theoretical analysis were combined into a multi-dimensional optimization program to optimize the design of high-power coreless stator AFPM generators in 2005 [5]. In 2006, the author of Reference [6] studied the torque ripple component of permanent magnet motors and proposed a method to minimize the torque ripple of surface permanent magnet motors. In order to ensure the reliability, safety, and ride comfort of the AFPMSM for electric vehicles, it is also possible to find an effective and reliable method from the control strategy. In Reference [7], a sliding mode vector control system based on cooperative control is established to drive AFPMSM. In Reference [8], the current control method is used to drive the AFPMSM, and internal model control was introduced. This paper focuses on the design and optimization of the AFPMSM for electric vehicles.

The design of AFPMSM usually requires 3D finite element method (FEM) analysis. Considering that multiple design variables need to be analyzed simultaneously, the time to design AFPMSM is significantly increased. The analytical algorithms to simplify analysis time are used to solve this problem [9–11]. A surrogate assisted multi-objective optimization algorithm was applied to significantly

reduce function calls, effectively reducing motor design time [9]. Under the same magnetic energy of the two models' permanent magnets, an AFPM motor is equivalent to a linear synchronous permanent magnet motor [10]. In order to obtain the key parameters of accurate surface mount permanent magnet synchronous motors, an analysis model based on Maxwell's equation and magnetic equivalent circuit was introduced [11]. The analysis algorithm can effectively reduce the development time when designing the motor. The AFPMSM for electric vehicles has a complicated structure, and the use of FEM will greatly increase the analysis time. For AFPMSM, its structure is complex, and the analytical algorithm can effectively reduce the development time in motor design. Therefore, the electromagnetic design method based on analytical formula studied in this paper has certain advantages.

Similar to RFPMSMs, AFPMSMs also have a torque ripple problem during operation. The existence of torque ripple will cause torsional vibration of the transmission system, which will adversely affect the motor control and torque output quality. Therefore, it is necessary to analyze and optimize its torque characteristics. The authors of Reference [12,13] optimized the torque ripple from the control method. The authors of Reference [14,15] optimized the torque ripple from the motor itself. In this paper, the stator core was used to open the auxiliary slot to optimize the torque ripple.

In recent years, AFPMSM's multi-physics analysis has also made great progress. The authors of Reference [16–18] used the steady-state heat conduction equation method, the T-type thermal network model method, and the AFPMSM full prediction heat transfer coefficient model with magnet geometry parameters to perform thermal analysis on AFPMSM. The authors of Reference [19–22] conducted a detailed study of the AFPMSM's degaussing fault identification. The method was proposed for detecting and locating asymmetric demagnetization defects in AFPMSM, which can be used for real-time condition monitoring of demagnetization defects or as a virtual temperature sensor for magnets. [19]. A time harmonic analysis model was proposed to study the demagnetization and rotor eccentricity of a single stator dual rotor AFPMSM [20]. A forward model was established for demagnetization detection of an AFPMSM. [21]. In addition, the eddy current losses of AFPMSMs have been analyzed in detail in Reference [22–24]. Because electric vehicles require high system efficiency, strong system environment adaptability and low noise, based on these characteristics, the current study analyzed and checked the vibration noise and temperature rise of several key operating conditions of automotive AFPMSMs based on multi-physics analysis software to ensure that the motor can always run smoothly.

In summary, this paper covers the study and design of a dual-stator-single-rotor structure of the new energy vehicle traction AFPMSM (the motor parameters are shown in Table 1; the motor structure diagram is shown in Figure 1). The AFPMSM for electric vehicles was based on a fast electromagnetic design method based on analytical formulas and a refined optimization design simulation technology based on machine-electric-thermal-structure multi-physics analysis, providing a complete solution for designing and optimizing AFPMSM for electric vehicles.

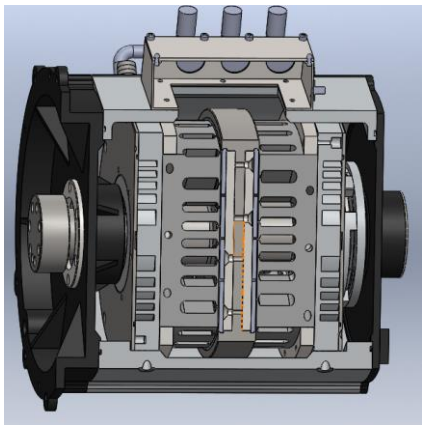

Figure 1. Double stator-single rotor type axial flux permanent magnet synchronous motor (AFPMSM).

Table 1. Motor parameters.

Motor Parameters	Symbol	Value
Pole-pairs	p	6
Slot number	Q	27×2
Air gap length	δ	1 mm
Rated torque	T_N	300 Nm
Rated power	P_N	50 kW
Stator outer diameter	D_{so}	250 mm
Phase number	m	3
Rated speed	n	1600 rpm
Permanent magnet Remanence	B_r	1.089 T
Coercivity	HC	2 A/m

2. Magnetic Path Analysis Algorithm for AFPMSM

2.1. Modeling and Analysis of Magnetic Circuit Analysis Algorithm

The AFPMSM has a unique magnetic circuit structure, and its electromagnetic design is quite different from that of the RFPMSM. In this paper, the model of AFPMSM was simplified by the 2D multi-loop equivalent method. Based on this, the magnetic circuit analysis algorithm was used to design the motor and obtain the electromagnetic parameters of the motor. The specific method is as follows. Take the motor stator N different diameters and expand it into a linear motor, and then superimpose the simulation results of N linear motors to get the final result, as shown in Figure 2. The radius D_{iave} taken by the i-th linear motor is as follows:

$$D_{iave} = D_{out} - \frac{2i-1}{N}\frac{D_{out} - D_{in}}{2}, i = 1, 2, \cdots, N \quad (1)$$

where D_{out} and D_{in} are the outer diameter and inner diameter of the stator.

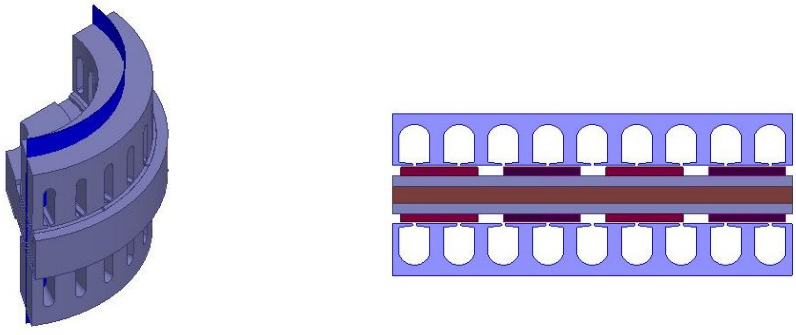

(**a**) (**b**)

Figure 2. Double stator-single rotor type AFPMSM. (**a**) AFPMSM 3D model. (**b**) Equivalent linear motor model.

When calculating the value of the electromagnetic field under ideal conditions, take $N = 1$. When calculating the loss and other information, take $N > 1$.

Then, use the equivalent magnetic network circuit as shown in Figure 3 to calculate the key electromagnetic parameters of the motor. In Figure 3, R_y is the equivalent reluctance of the stator yoke, R_t is the magnetic reluctance of the tooth, F_l is the magneto motive force generated by the stator winding, R_s is the slot reluctance, R_g is the air gap reluctance, and F_{PM} is the magneto motive force generated by the permanent magnet.

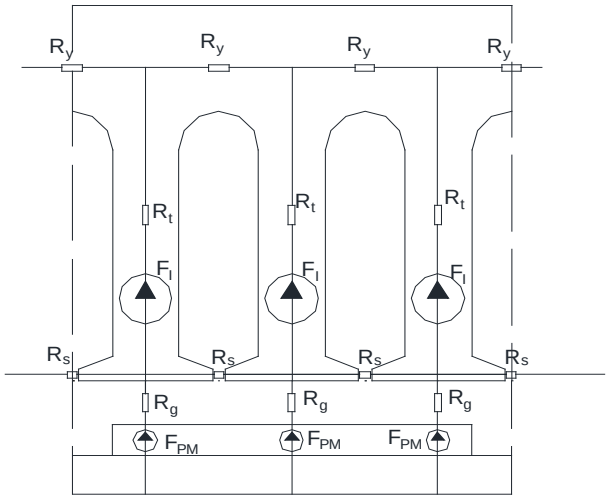

Figure 3. Equivalent magnetic network model of the AFPMSM.

The AFPMSM is equivalent to a linear motor in this paper, and the magnetic circuit analysis method (MCAM) model was used to analyze the air gap magnetic density distribution of AFPMSM [25–28]:

$$B_{mg}(r,x) = \sum_{n=1,3,5,\cdots}^{\infty} \frac{-\frac{8B_r}{n\pi}\sin\left(\frac{\alpha_p(r)n\pi}{2}\right)e^{\frac{-n\pi g'}{\tau_p(r)}}\cos\left(\frac{n\pi x}{\tau_p(r)}\right)}{\left(e^{\frac{-n\pi g'}{\tau_p(r)}}+1\right)+\frac{\mu_{PM}\left(e^{\frac{-n\pi g'}{\tau_p(r)}}+1\right)\left(e^{\frac{2n\pi l_{PM}}{\tau_p(r)}}+1\right)}{\mu_0\left(e^{\frac{2n\pi l_{PM}}{\tau_p(r)}}-1\right)}} \tag{2}$$

where r is the radius and x is the perimeter at different radii and is equal to $2\pi r$. $\tau_p(r)$ is the pole pitch of the permanent magnet when the radius is r, and $\tau_p(r) = \pi r/p$. $\alpha_p(r)$ is the polar arc coefficient when the radius is r, and $\alpha_p(r) = w_{PM}(r)/\tau_p(r)$, where $w_{PM}(r)$ is the width of the permanent magnet when the radius is r. l_{PM} is the thickness of the permanent magnet, μ_0 is the vacuum permeability, μ_{PM} is the permanent magnet permeability, and g' is the air gap length.

Since the open slot affects the air gap flux density, the air gap permeability function $\lambda(x)$ is introduced to consider the effect of the open slot on the air gap flux distribution. The air gap magnetic density distribution $B_{mag}(r,x)$ including the slotting effect is

$$B_{mag}(r,x) = \lambda(x)B_{mg}(r,x) \tag{3}$$

when the motor is used as a drive motor; the no-load phase voltage is generated only by the flux generated by the permanent magnet. According to Equations (2) and (3), it can be calculated as:

$$e_{i,PM} = -N_{ph}k_{db}\frac{\Delta\Phi_{i,PM}}{\Delta t} \tag{4}$$

where N_{ph} is the number of turns in series for each phase, K_{db} is the fundamental winding factor, and $\Phi_{i,\,PM}$ is the air gap flux obtained by numerical integration of the air gap flux density distribution,

$$\Phi_{i,PM} = \int_0^{\tau_{p,i}}\int_0^{\frac{l_s}{N}} B_{agap,i}(x)dxdl \tag{5}$$

where $\tau_{p,i}$ is the permanent magnet pole pitch of the i-th equivalent plane, l_s is the length of the stator punch and $l_s = (D_{out}-D_{in})/2$, and $B_{agap,i}(x)$ is the air gap magnetic density function in the i-th equivalent plane.

Therefore, the no-load back electromotive force (EMF) of the AFPMSM is

$$e_{PM}(t) = \sum_{i=1}^{N} e_{i,PM}(t) \tag{6}$$

This paper presents a method to reduce the cogging torque. The cogging torque is calculated from the no-load air gap flux density distribution. Assume that the cogging torque of the axial flux motor unit is

$$T_{cog,i}(\theta) = \frac{\partial W}{\partial \theta} = \frac{\partial \left(\iiint_V B_{agap,i}^2 dV \right)}{2\mu_0 \partial \theta} \tag{7}$$

where V is the air gap volume, θ is the rotor position angle, and W is magnetic energy.

During calculation of the cogging torque, it is assumed that the magnetic flux density distribution of each axial flux motor unit does not change in the radial direction. Analogizing the back EMF calculation, the cogging torque generated by the axial flux motor is

$$T_{cog}(\theta) = \sum_{i=1}^{N} T_{cog,i}(\theta) \tag{8}$$

2.2. Comparative Analysis of MCAM and 3D FEM

As described in Section 2.1, based on Matrix Laboratory programming, the magnetic circuit analysis method compared with the finite element method as follows.

The air gap magnetic density of the motor has a crucial influence on the saturation degree of the motor, the output power requirement, and the loss level. Therefore, it is important to analyze the air gap magnetic density of the AFPMSM. Figure 4 shows that the air-gap magnetic density distribution waveforms calculated by the FEM and the MCAM are basically the same, and the FEM can more accurately consider the cogging and magnetic flux leakage of the motor, so the calculation accuracy is higher than the analytical method. However, the MCAM takes a short time and can be used for screening the initial design of the AFPMSM.

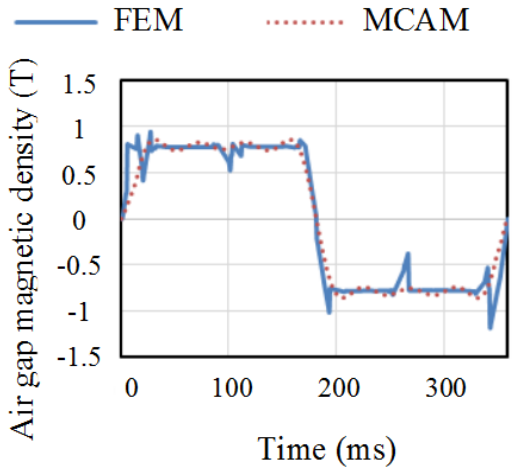

Figure 4. No-load air gap magnetic density of AFPMSM.

Figure 5 is a comparison of the analytical results of the FEM and MCAM of the AFPMSM back EMF. It can be seen from Figure 6a,b that the MCAM has omissions in the analysis of the third harmonic magnetic density, and the analysis results of the fundamental wave and other harmonics are in good agreement with the finite element method.

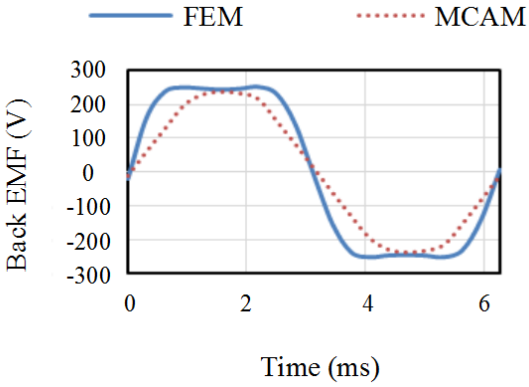

Figure 5. No-load back electromotive force (EMF) of the AFPMSM.

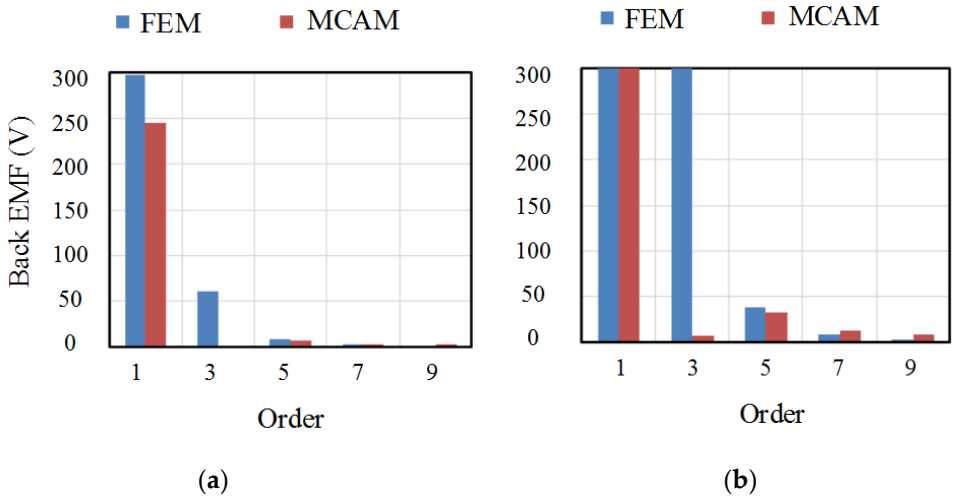

Figure 6. Comparison of back-EMF harmonic analysis results of the AFPMSM. (**a**) Overall picture. (**b**) Partial enlargement picture.

Figure 7 shows that that the MCAM is basically consistent with the analysis of the positioning torque and the finite element analysis results, and the maximum amplitude difference is 0.2 Nm, which satisfies the initial design accuracy requirements of the motor.

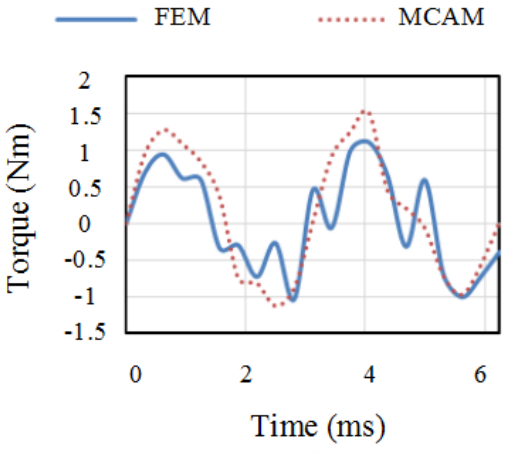

Figure 7. Analysis of positioning torque of AFPMSM.

In summary, the air gap magnetic density, the no-load back EMF, and the positioning torque calculated by the FEM and the MCAM are basically the same. Since the FEM can fully consider the

motor cogging effect and the magnetic flux leakage coefficient, the accuracy is higher than the MCAM. However, when the distribution trend is basically the same, the time used by the MCAM is much less than that of the FEM. Therefore, the MCAM studied in this paper can be used to screen the initial design of the AFPMSM.

3. Torque Ripple Optimization of AFPMSM

Electric vehicles generally operate in torque mode. The output of the motor torque is controlled according to the depth at which the driver steps on the throttle. The presence of torque ripple adversely affects the torque output. Therefore, the torque ripple needs to be optimized. The effect of opening the auxiliary slot on the motor stator on the torque ripple is equivalent to increasing the number of armature slots, i.e., changing the pole slot fit. If the position and size of the open auxiliary slot are properly selected, the torque ripple of the motor can be weakened. First, theoretical analysis is used to determine the number of auxiliary slots, slot width, and position distribution on each tooth, and then the slot depth is continuously adjusted in the three-dimensional simulation. The slot depth should suppress the torque ripple as much as possible without affecting the performance of the motor. The number of auxiliary slots is derived below. The motor in this paper has 12 poles and 27 slots. According to the literature [23]:

$$\{i(k+1)\big|i \in N^*\} \tag{9}$$

$$\left\{i \cdot \frac{2p}{GCD(z,2p)}\middle| i \in N^*\right\} \tag{10}$$

where p is the pole pairs, z is the number of stator slots, and $GCD(z, 2p)$ is the greatest common divisor (GCD) of z and $2p$.

To attenuate torque ripple, the number k of stator toothed auxiliary slots should be such that the intersection of set (9) and set (10) is reduced. The AFPMSM studied in this paper has $p = 6$, $z = 27$, and $k = 2$, so the two sets are {3, 6, 9 . . . } and {4, 8, 12 . . . }. Obviously, there is no intersection between the two sets, so the torque ripple is significantly reduced compared to the absence of the auxiliary slot. If $k = 1$, the intersection of the above two sets is {4, 8, 12 . . . }. In summary, $k = 2$ and the width of the auxiliary slot is equal to the slot width.

In summary, the motor of the present invention opens two auxiliary slots, the auxiliary slots are evenly distributed on the stator teeth, and the width of the auxiliary slots is the same as the width of the stator slots. The finite element analysis model is shown in Figure 8a, and a partial enlarged view of the auxiliary slot is shown in Figure 8b.

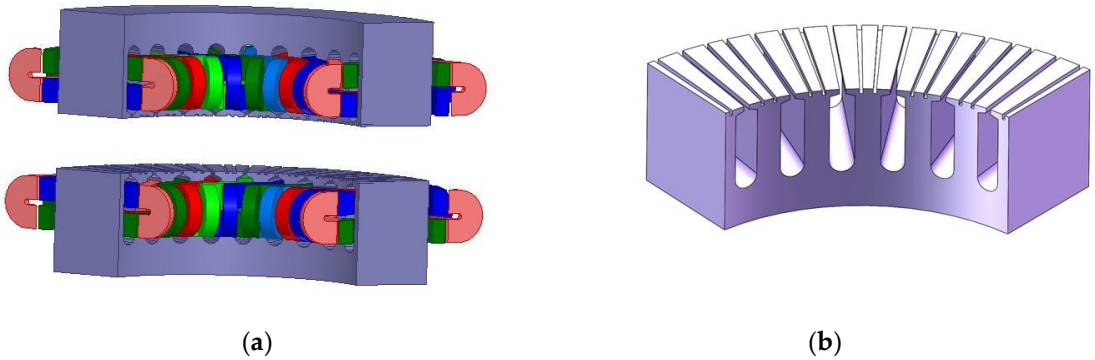

(**a**) (**b**)

Figure 8. AFPMSM auxiliary slot schematic. (**a**) Finite element analysis model. (**b**) Partial enlarged view of the auxiliary slot.

In order to verify the feasibility of opening the auxiliary slot to suppress the torque ripple, this section analyzes the load back EMF and load torque of constant torque maximum speed operating point and constant power zone maximum speed operating point under rated load and peak load before

and after optimization. The maximum speed of the constant torque is 1600 rpm, and the maximum speed of the constant power is 3000 rpm.

3.1. Comparative Analysis of Rated Load Characteristics at 1600 rpm

Under rated load conditions, it can be seen from Figure 9 that the third, fifth, seventh, and ninth harmonics of the load back electromotive force of the auxiliary slot method are weakened when the rotational speed is 1600 rpm; the weakening of the fifth and seventh harmonics is more significant.

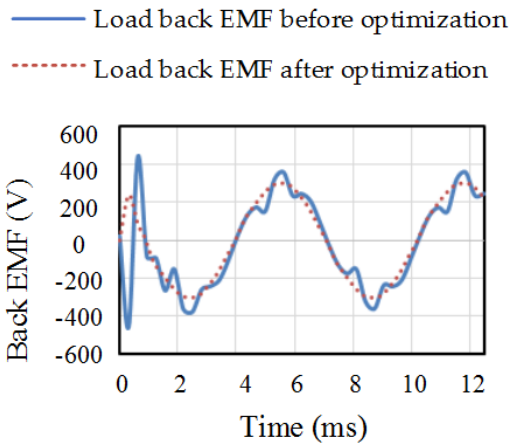

Figure 9. Back EMF of the AFPMSM at the rated load.

Figure 10 shows that when the rotation speed is 1600 rpm, the peak-to-peak load torque of the auxiliary slot method is 10 Nm, and the peak-to-peak value of the load torque without the auxiliary slot method is 16 Nm. The peak-to-peak value of the torque ripple after opening the auxiliary slot is reduced by about 4%, so the optimization method of opening the auxiliary slot at rated load can effectively attenuate the torque ripple under constant torque conditions.

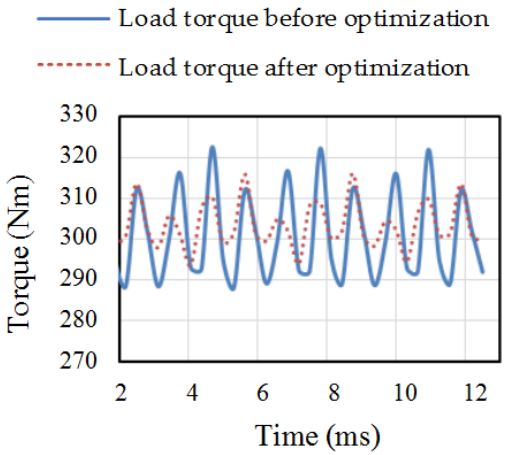

Figure 10. Torque of the AFPMSM at the rated load.

3.2. Comparative Analysis of Peak Load Characteristics at 1600 Rpm

Under the peak load condition, it can be seen from Figure 11 that the seventh and ninth harmonics of the load back electromotive force of the auxiliary slot method are weakened when the rotation speed is 1600 rpm; the third and fifth harmonics are higher than the no auxiliary slot method.

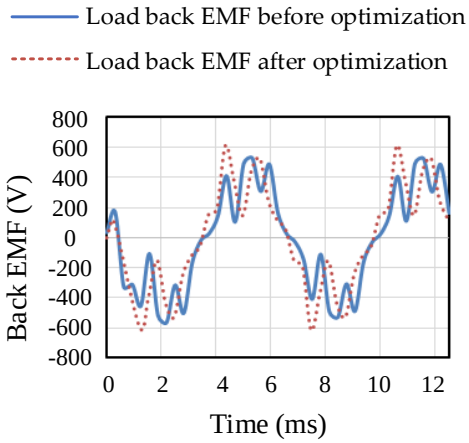

Figure 11. Back EMF of the AFPMSM at the peak load.

Figure 12 shows that the load torque peak-to-peak value of the open auxiliary slot method is 26 Nm when the rotation speed is 1600 rpm, and the load torque peak-to-peak value of the no auxiliary slot method is 32 Nm. The torque ripple of the open auxiliary slot method is reduced by about 2%, so the optimization method of opening the auxiliary slot at the peak load can also effectively attenuate the torque ripple under constant torque conditions.

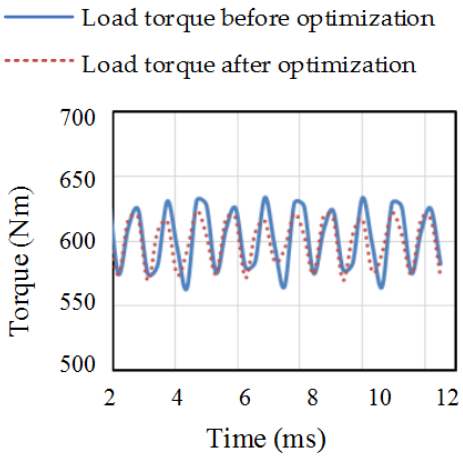

Figure 12. Torque of the AFPMSM at the peak load.

3.3. Comparative Analysis of Rated Load Power Characteristics at 3000 rpm

Under the rated load condition, as can be seen from Figure 13, when the rotational speed is 3000 rpm, the fifth, seventh, and ninth harmonics of the load back EMF of the auxiliary slot method are all weakened; the weakening of the fifth, seventh, and ninth harmonics is more significant.

Figure 14 shows that the load torque peak-to-peak value of the auxiliary slot optimization method is 3.5 Nm when the rotation speed is 3000 rpm, and the peak-to-peak value of the load torque before optimization is 10 Nm. The torque ripple of the auxiliary slot method is reduced by about 4%, so the torque ripple optimization method of the auxiliary slot can effectively attenuate the load torque ripple under constant power conditions.

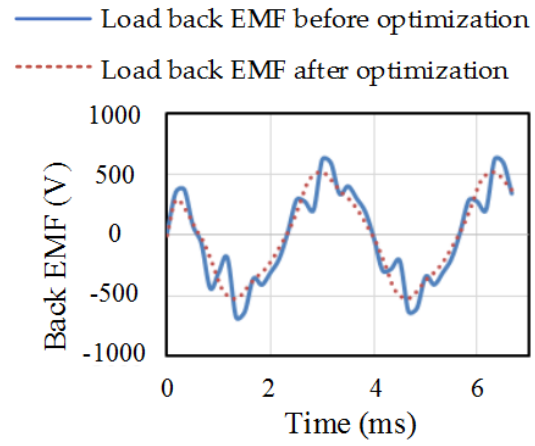

Figure 13. Back EMF of the AFPMSM at the rated load power.

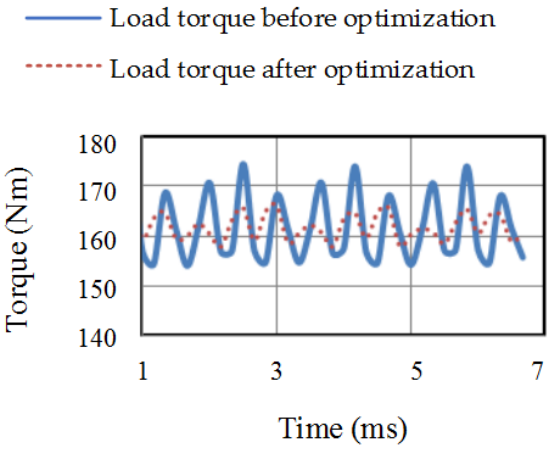

Figure 14. Torque of the AFPMSM at the rated load power.

3.4. Comparative Analysis of Peak Load Power Characteristics at 3000 rpm

Figure 15 shows that the load back EMF waveform is significantly optimized under the peak load power speed of 3000 rpm. Figure 16 shows that the load torque peak-to-peak value of the auxiliary slot optimization method is 10 Nm when the rotation speed is 3000 rpm, and the peak-to-peak value of the load torque before optimization is 16 Nm. The torque ripple of the auxiliary slot method is reduced by about 2%. Therefore, the torque ripple optimization method of the auxiliary slot can effectively attenuate the load torque ripple under constant power conditions and peak load conditions.

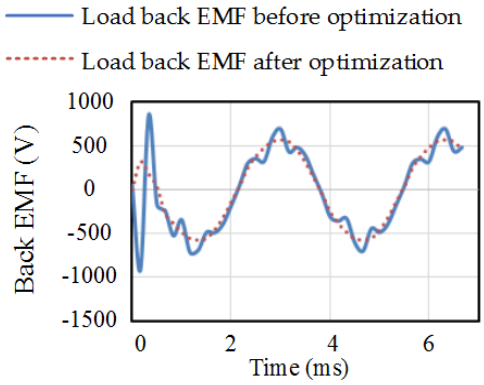

Figure 15. Back EMF of the AFPMSM at the peak load power.

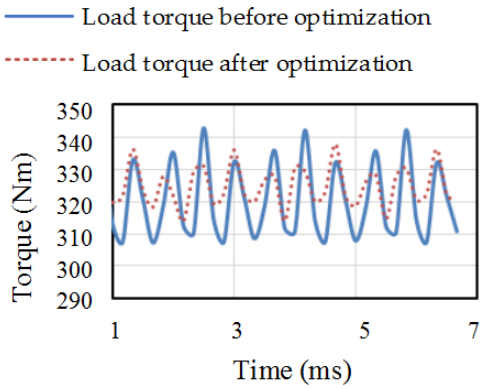

Figure 16. Torque of the AFPMSM at the peak load power.

In summary, at the constant torque maximum speed operating point, the rated load and peak load torque ripple ratio are reduced by 4% and 2%, respectively, before optimization. At the constant power maximum speed operating point, the rated load and peak load torque ripple are reduced by 4% and 2%, respectively, before optimization. Therefore, the AFPMSM opening auxiliary slot can effectively weaken the torque ripple of the motor, which is a reference for scholars studying the axial flux motor optimization design.

4. Multi-Physics Analysis

The traction motor of electric vehicle pursues high density and light weight in its design, and the working environment is complex and changeable. This is easy for causing electromagnetic noise and excessive temperature rise, which affects the reliability, safety and ride comfort of the whole vehicle. Therefore, multi-physics analysis of the motor is required. Controlling the electromagnetic noise within a certain range can improve the ride comfort; in addition, the heating problem of the motor directly affects the safety and reliability of the drive system, so thermal analysis of the motor is necessary. Figure 17 shows the finite element simulation model obtained and optimized above.

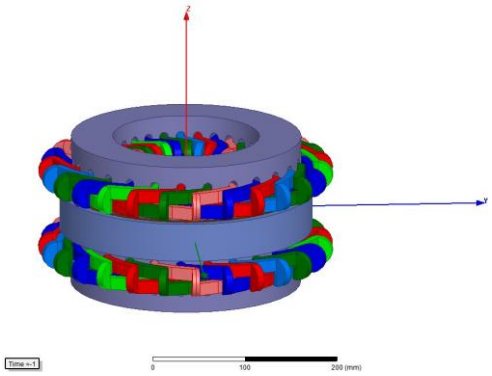

Figure 17. AFPMSM finite element simulation model.

The stator and rotor structure of AFPMSM is different from the traditional RFPMSM. In order to ensure the comprehensiveness of the analysis, the electromagnetic interference generated by the electromagnetic force of the stator and the electromagnetic force of the rotor is analyzed.

4.1. Electromagnetic Noise Generated by the AFPMSM Stator Structure

Firstly, a 3D finite element modal simulation model of the AFPMSM stator structure was established. The stator core structure has an elastic modulus of 205 GPa, a Poisson's ratio of 0.27 and a

density of 7305 kg/m^3. Figure 18 shows the stator structure finite element simulation model and mesh segmentation diagram.

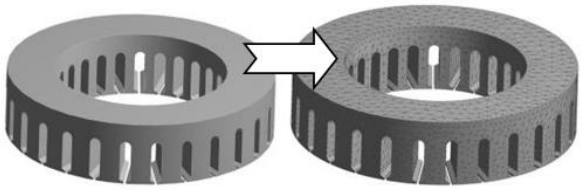

Figure 18. Finite element simulation model of the stator core.

In the finite element modal calculation, the AFPMSM stator model uses the additional mass method to make the winding end equivalent to a ring, thus calculating the natural frequency of the motor stator. The AFPMSM stator structure mode shape obtained by simulation is shown in Figure 19, and the modal frequency is shown in Table 2. It can be seen from Table 2 that using the winding as an additional mass analysis stator mode can increase the stiffness of the stator, increase the frequency range, and reduce the possibility of motor resonance.

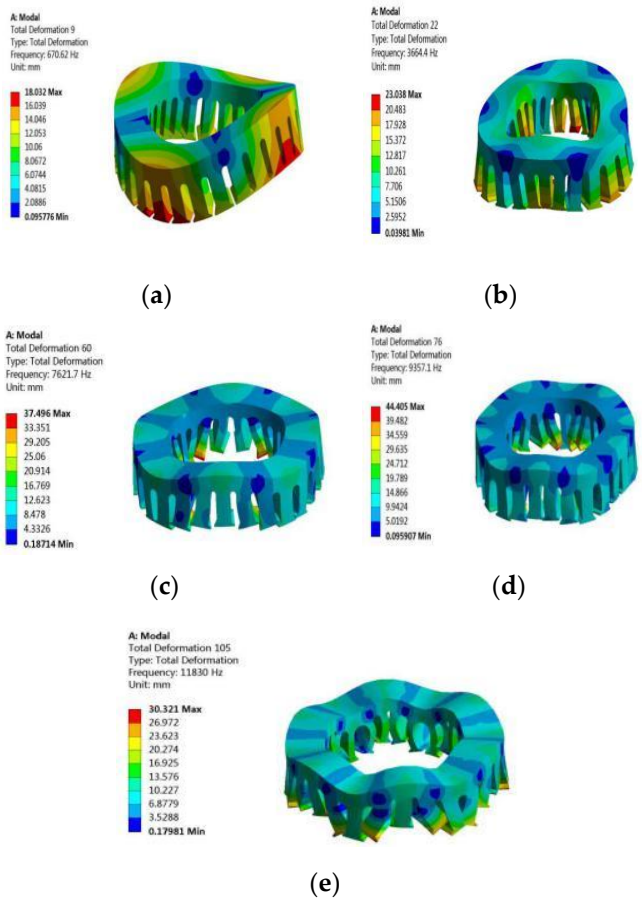

Figure 19. Finite element simulation model of the stator core. (**a**) Second order model. (**b**) Third order model. (**c**) Fourth order model. (**d**) Fifth order model. (**e**) Sixth order model.

Table 2. Modal frequency of stator core (Hz).

Modal Order	Order 2	Order 3	Order 4	Order 5	Order 6
Frequency	671	3664	7621	9357	11,830

The air domain model of motor electromagnetic noise radiation is established by A-weighting. The radiation characteristics of motor noise are analyzed based on the cylindrical air domain model. The results of sound pressure level analysis at each frequency are shown in Figures 20 and 21.

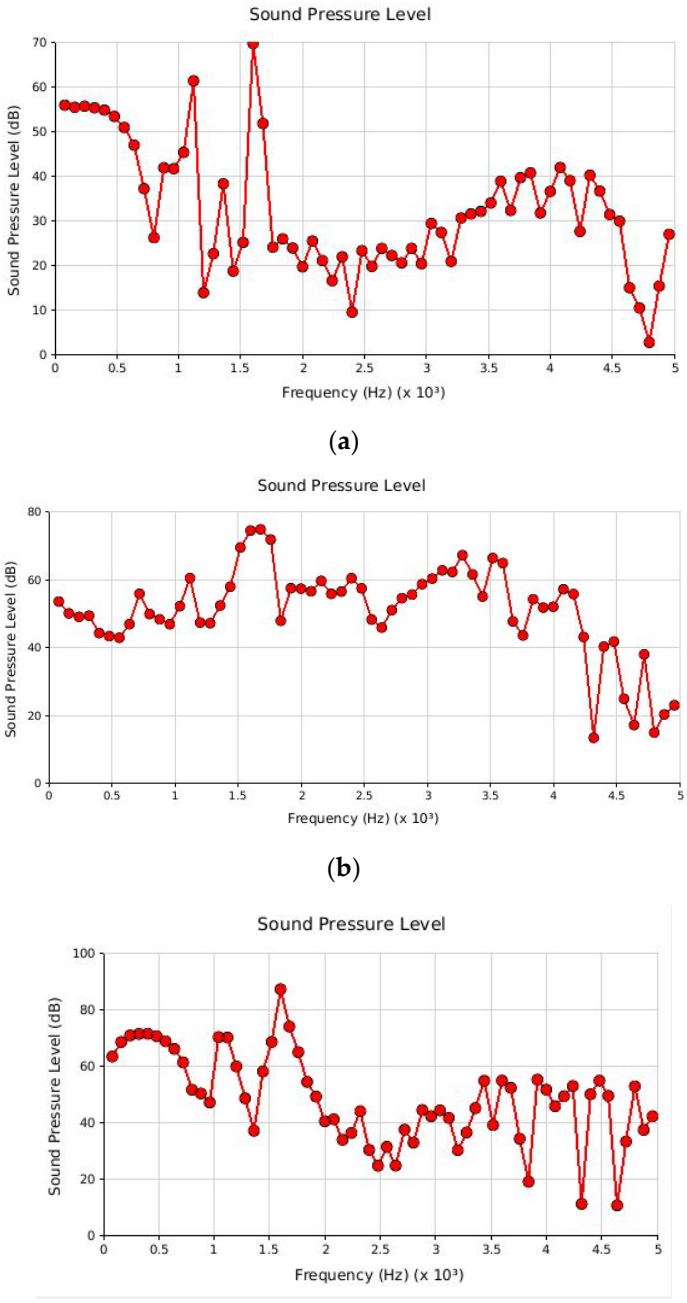

Figure 20. Stator system electromagnetic noise at 1600 rpm. (**a**) Electromagnetic noise at no load. (**b**) Electromagnetic noise at rated load. (**c**) Electromagnetic noise at peak load.

The sound pressure level of the electromagnetic noise at each working point of the motor can be calculated by the sound pressure level summation formula, as shown below:

$$L = 10\lg(\sum_{i=1}^{n} 10^{0.1L_i}) \tag{11}$$

where L_i is the sound pressure level value at the frequency and n is the number of frequency points.

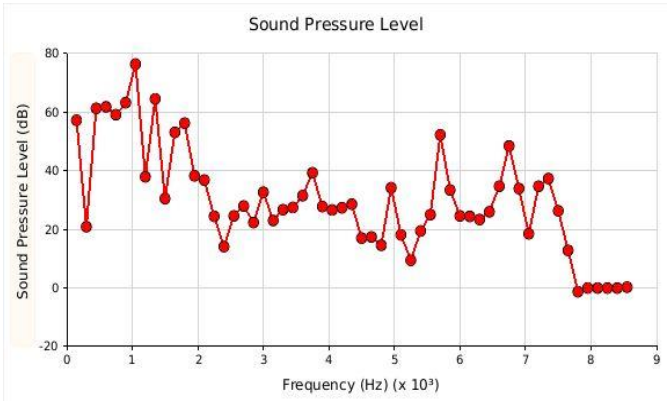

(**a**)

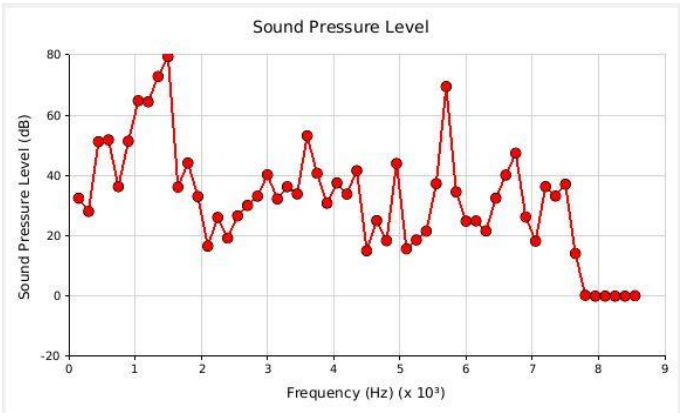

(**b**)

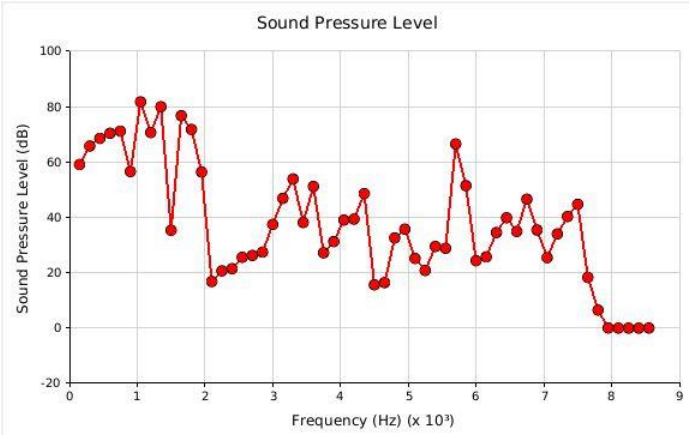

(**c**)

Figure 21. Stator system electromagnetic noise at 3000 rpm. (**a**) Electromagnetic noise at no load. (**b**) Electromagnetic noise at rated load. (**c**) Electromagnetic noise at peak load.

According to the sensitive range of the human ear to frequency, the sound pressure components in the range of 0 to 6000 Hz were selected for summation. The electromagnetic noise of the no-load, rated load, and peak load of the motor 1600 r/min were calculated to be 71 dB, 80 dB, and 88 dB, respectively; the electromagnetic noise of no-load, rated load, and peak load of 3000 r/min are 77 dB, 81 dB, and 86 dB respectively. The peak load noise of the motor 3000 r/min is large, but the torque required by the general vehicle during high-speed cruising is not large, therefore, the electromagnetic

noise of the working point has little effect on the performance of the whole vehicle, and certain sound-absorbing or sound-insulating materials can be used for noise reduction processing.

4.2. Electromagnetic Noise Generated by the AFPMSM Rotor Structure

The finite element modal simulation model of the automotive AFPMSM rotor structure was established, and the natural frequency and vibration mode of the rotor structure were obtained, as shown in Figure 22.

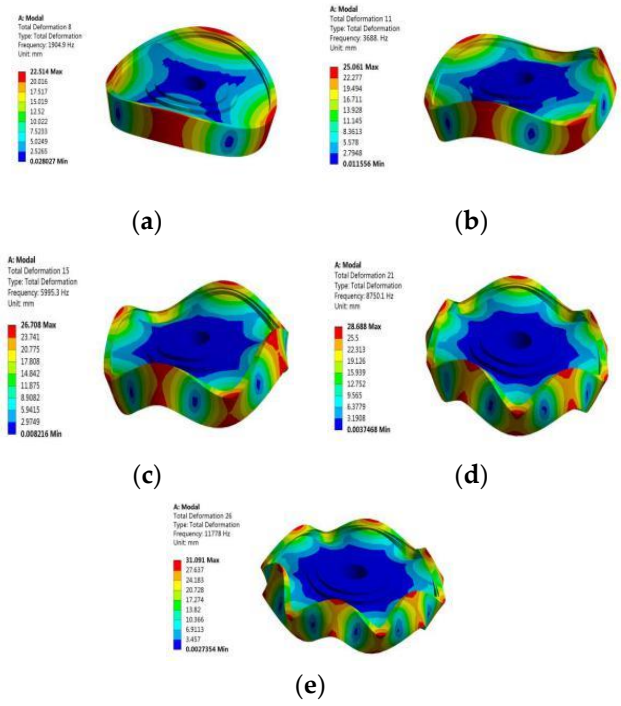

Figure 22. Rotor core axial flux mode shape. (**a**) Second order model. (**b**) Third order model. (**c**) Fourth order model. (**d**) Fifth order model. (**e**) Sixth order model.

The natural frequencies of the second-order mode and the third-order mode of the rotor of the AFPMSM are 1905 Hz and 3688 Hz, respectively, and the generated electromagnetic vibration amplitude is small, so electromagnetic vibration does not cause large vibration noise.

The electromagnetic noise of the rotor structure of the motor was simulated, and the noise sound pressure level results of the respective frequency components were obtained as shown in Figures 23 and 24. Since the peak load electromagnetic noise is greater than the rated load electromagnetic noise, the rotor section only shows the electromagnetic noise under peak load conditions.

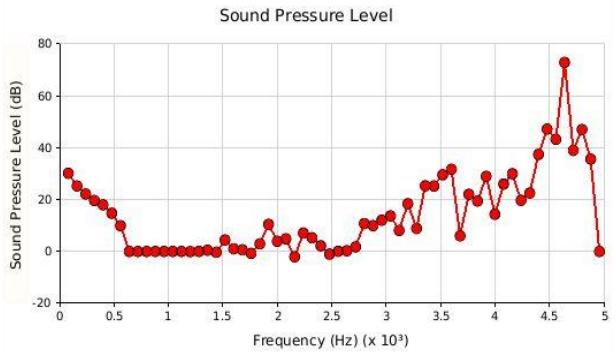

Figure 23. Peak load electromagnetic noise at 1600 rpm.

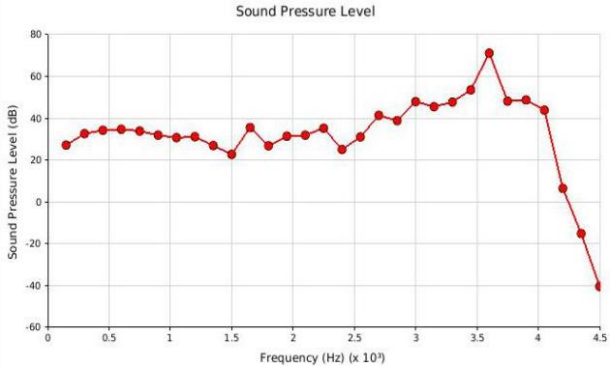

Figure 24. Value-loaded electromagnetic noise at a speed of 3000 rpm.

Calculated by Formula (11), the peak load electromagnetic noise of 1600 r/min is 72 dB; the peak load electromagnetic noise of the motor speed of 3000 r/min is 71 dB. The electromagnetic noise generated by the stator structure is the main source of AFPMSMs.

When the electromagnetic performance of the vehicle motor was evaluated, the magnetic field saturation of the constant torque working point was the largest, and the magnetic field distortion of the working point of the constant power maximum speed was the largest, which is the typical working condition of the traction motor for the vehicle. Therefore, the maximum speed operating point of the constant torque zone and the maximum speed operating point of the constant power zone are often selected as the key working points of the electromagnetic performance. In summary, the rated load and peak load electromagnetic noise of the stator structure at the constant torque operating point are 80 dB and 88 dB, respectively, and the rated load and peak load electromagnetic noise at the constant power maximum speed operating point are 81 dB and 86 dB, respectively. The peak load electromagnetic noise of the rotor structure at the constant torque operating point is 72 dB, and the peak load electromagnetic noise at the constant power maximum speed operating point is 71 dB. According to biology, the sound range that does not affect human health ranges from 0 to 90 dB. The maximum noise of the motor designed in this paper is 88 dB, which is within a reasonable range.

5. Thermal Analysis of AFPMSM

The problem of heating and cooling of the motor for vehicles directly affects the safety and reliability of the drive system. The accurate prediction of the temperature rise of the motor and the design of the efficient cooling system are of great significance to the safety and reliability of the new energy vehicles.

5.1. AFPMSM Temperature Field Equivalent Simplified Calculation Model

To simplify the analysis, an equivalent model of the stator winding was established, introducing an equivalent conductor that replaced the winding copper wire and an equivalent insulating layer of all the insulating materials in the slot, as shown in Figure 25.

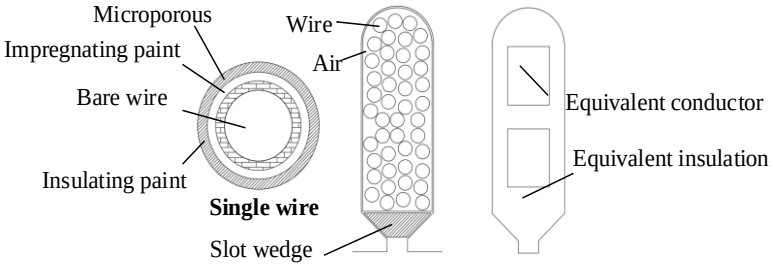

Figure 25. Equivalent winding model.

The equivalent thermal conductivity of the slot insulation is calculated as

$$\lambda_{eq} = \sum_{i=1}^{n} d_i / \left(\sum_{i=1}^{n} \frac{d_i}{\lambda_i} \right) \tag{12}$$

where λ_{eq} is the equivalent thermal conductivity of the insulating material, d_i is the equivalent thickness of each insulating material in the groove, λ_i is the thermal conductivity of the corresponding insulating material.

The AFPMSM in this paper uses a fully enclosed end cap cooling structure. To simplify the analysis, the following assumptions were made:

1. The insulating paint of the winding is evenly distributed, and the winding is completely dip-coated;
2. Since the inter-strand insulation of the armature windings cannot be completely considered and wound, the inner region of the stator slots is equivalently treated. The cross-sectional areas of the upper and lower windings are equal, and the thickness of the insulating layer, the windings and the left and right sides, and the windings of the windings and the upper and lower sides are equal;
3. Ignoring radiation heat dissipation and contact thermal resistance between the rotor and the rotating shaft;
4. The loss of each part of the motor does not change with temperature;
5. The heat generated by the heat source is mainly carried away by the end cover cooling water, and the heat exchange between the outer surface of the casing and the surrounding air is negligible.

The solution domain model of the motor based on the above assumptions is shown in Figure 26.

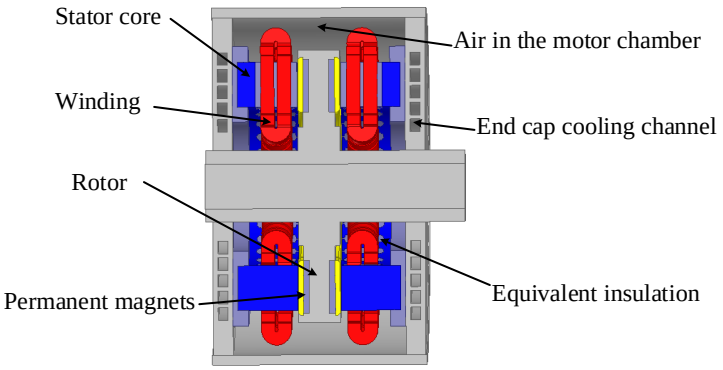

Figure 26. Motor temperature field solution domain model.

The axial flux motor is meshed, and the split model of each part of the motor is shown in Figure 27. The whole motor is divided into 17,346,364 individual cell grids and 3,412,225 nodes.

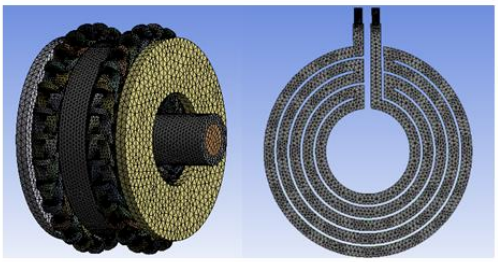

Figure 27. Schematic diagram of the prototype fluid-solid coupling simulation model.

5.2. Temperature Field Analysis under AFPMSM Rated Conditions

Thermal simulation of the motor was conducted based on ANSYS/Workbench. The inlet water flow rate was 0.8 m/s, the ambient temperature was 30 °C, and the inlet coolant temperature was 25 °C. The rated torque operating point of 50 kW and 1600 r/min was selected, and the motor temperature distribution as shown as Figure 28 is when the motor reached the thermal steady state for a long time.

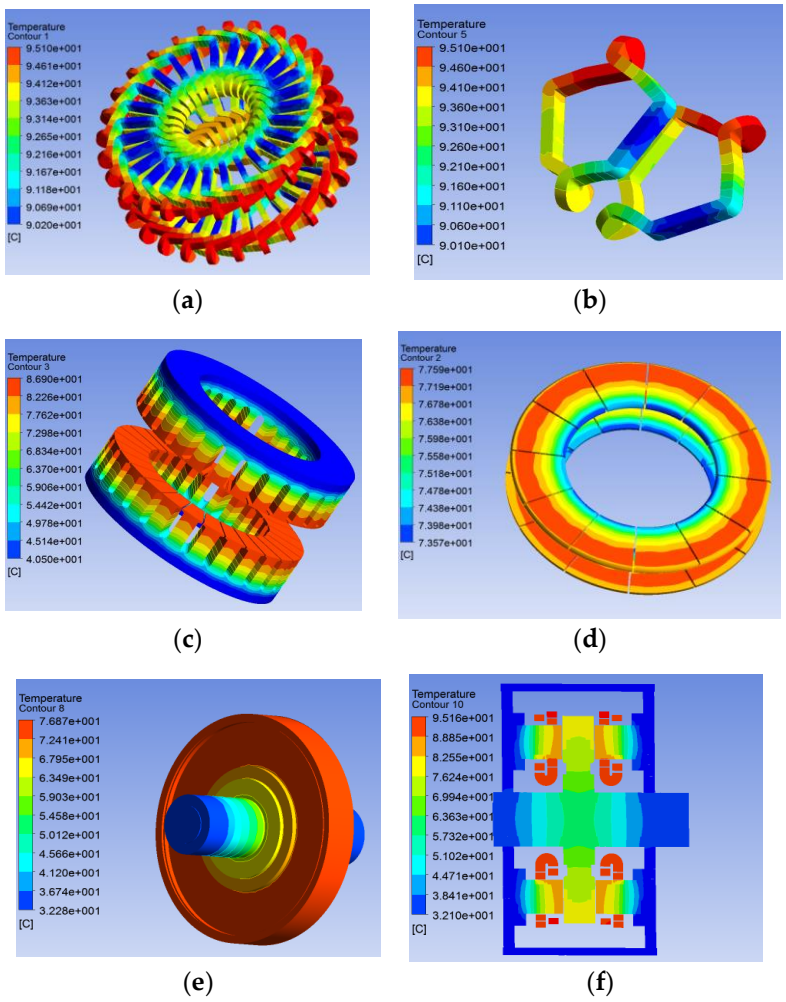

Figure 28. Temperature map of each part of the AFPMSM. (**a**) Winding temperature cloud map. (**b**) Upper and lower winding temperature cloud map. (**c**) Stator core temperature cloud map. (**d**) Permanent magnet temperature map. (**e**) Rotor and shaft temperature cloud map. (**f**)Whole machine section temperature cloud map.

As seen from the thermal simulation results, the temperature rise at the end of the stator winding is high. There is a direct temperature difference between the upper and lower windings in the same slot, and the temperature near the stator yoke winding is lower. The temperature of the stator teeth is significantly higher than the stator yoke. The temperature at the outer diameter of the permanent magnet is significantly higher than the inner diameter. The maximum temperature of the motor appears at the outer end of the winding (near the casing) at 95 °C. The maximum temperature of the stator core is the stator tooth at 87 °C. The maximum temperature of the permanent magnet is at the outer diameter of the permanent magnet at 78 °C. The internal temperature of the whole machine is, from the highest to the lowest, the winding end, the stator tooth, the permanent magnet, the rotor disk, the stator disk, and the casing. The analysis shows that the temperature rise of the motor's long-term rated operation is within a reasonable range, and the motor can operate safely and reliably.

5.3. Temperature Field Analysis of AFPMSM under Peak Operating Conditions

Considering the operating conditions of the actual electric vehicle, the temperature rise of the motor is further checked by operating the peak torque for 60 s after assuming that the rated operation of the motor reaches a thermal steady state. The temperature rise of the motor components over time during the 60 s operation of the motor with peak torque is shown in Figure 29.

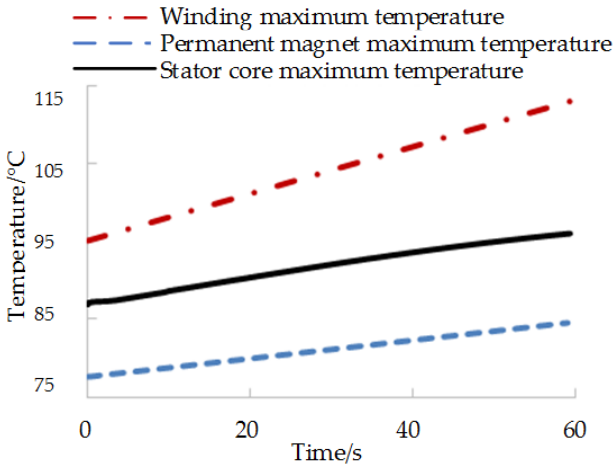

Figure 29. Temperature of main components of the motor changes with time.

Figure 29 shows that the winding temperature rises the fastest when the motor peak torque is running, and the maximum temperature of the winding reaches 113 °C after running for 60 s, which is 18 °C higher than the rated working temperature; the maximum temperature of the stator core is 95.9 °C, which is 9 °C higher than the rated working condition. The maximum temperature of the permanent magnet is 84.68 °C, which is 7 °C higher than the rated working temperature. The winding temperature rises the fastest. Because the copper consumption of the peak torque condition is relatively large, the thermal conductivity of the insulating material is poor, and the generated heat is difficult to dissipate in a short time. In this paper, the motor uses H-class insulation. The results of motor thermal analysis show that the temperature rise of the motor meets the technical requirements.

6. Conclusions

This paper first proposes a 2D multi-loop equivalent method to simplify the AFPMSM model and, based on this, establishes the equivalent magnetic network model and air gap magnetic density distribution function of AFPMSMs. Secondly, by comparing the torque ripple values under multi-operating conditions before and after the open stator auxiliary slot, the feasibility of reducing the AFPMSM torque ripple is verified by the open stator auxiliary slot. Finally, the experimental results of AFPMSM in multi-physics such as vibration, noise, and temperature rise are obtained by finite element software and simulation experiments. The following conclusions can be drawn:

1. The electromagnetic design method based on the analytical method was used to analyze the key electromagnetic parameters such as air gap magnetic density harmonics, positioning torque and no-load back EMF of AFPMSM. The correctness of the analytical calculation was verified by 3D electromagnetic field simulation.
2. The stator core was used to open the auxiliary slot to suppress the torque ripple, and the maximum torque ripple peak-to-peak value was reduced by 2%.
3. Based on the multi-physics simulation software, the vibration and noise characteristics of the motor were analyzed from the electromagnetic force and the modal state. The electromagnetic noise characteristics of the no-load, rated load, and peak load operating points at different speeds were simulated. The noise, vibration and harshness (NVH) of the motor was verified.

4. The thermal simulation based on fluid-structure coupling checked the temperature rise of the AFPMSM after the rated operating point reached the thermal steady state and transient operation for 1 min, which ensured the safety and reliability of the motor running under vehicle working conditions.

In summary, the AFPMSM design and research method proposed in this paper verifies the superior performance of AFPMSM as a motor for vehicles. On the other hand, this paper provides a complete solution for the design and optimization of AFPMSMs for electric vehicles, which can provide relevant researchers with AFPMSM performance reference indicators.

Author Contributions: Conceptualization, J.Z., Y.D., and Q.H.; methodology, J.Z.; software, Q.H. and M.H.; validation, J.Z., Y.D., and Q.H.; formal analysis, J.Z. and Y.D.; investigation, Y.D. and M.H.; resources, J.Z.; data curation, Q.H. and M.H.; writing—original draft preparation, J.Z., Q.H., and Y.D.; writing—review and editing, J.Z. and Q.H.; visualization, Q.H. supervision, J.Z.; project administration, J.Z.; funding acquisition, J.Z.

Funding: This research was supported by 111 project, No. D18003.

Conflicts of Interest: The authors declare no conflict of interest.

References

1. Chen, Y.; Zhang, B. Minimization of the Electromagnetic Torque Ripple Caused by the Coils Inter-Turn Short Circuit Fault in Dual-Redundancy Permanent Magnet Synchronous Motors. *Energies* **2017**, *10*, 1798. [CrossRef]
2. Wang, W.; Wang, W. Compensation for Inverter Nonlinearity in Permanent Magnet Synchronous Motor Drive and Effect on Torsional Vibration of Electric Vehicle Driveline. *Energies* **2018**, *11*, 2542. [CrossRef]
3. Pietrusewicz, K.; Waszczuk, P.; Kubicki, M. MFC/IMC Control Algorithm for Reduction of Load Torque Disturbance in PMSM Servo Drive Systems. *Appl. Sci.* **2019**, *9*, 86. [CrossRef]
4. Jia, Y.F.; Chu, L.; Xu, N.; Li, Y.K.; Zhao, D.; Tang, X. Power Sharing and Voltage Vector Distribution Model of a Dual Inverter Open-End Winding Motor Drive System for Electric Vehicles. *Appl. Sci.* **2018**, *8*, 254. [CrossRef]
5. Wang, R.J. Optimal design of a coreless stator axial flux permanent-magnet generator. *IEEE Trans. Magn.* **2005**, *41*, 55–64. [CrossRef]
6. Aydin, M.; Huang, S.; Lipo, T.A. Torque quality and comparison of internal and external rotor axial flux surface-magnet disc machines. *IEEE Trans. Ind. Electron.* **2006**, *53*, 822–830. [CrossRef]
7. Zhao, J.F.; Hua, M.Q.; Liu, T.Z. Research on a Sliding Mode Vector Control System Based on Collaborative Optimization of an Axial Flux Permanent Magnet Synchronous Motor for an Electric Vehicle. *Energies* **2018**, *11*, 3116. [CrossRef]
8. Darba, A.; Esmalifalak, M.; Barazandeh, E.S. Implementing SVPWM technique to axial flux permanent magnet synchronous motor drive with internal model current controller. In Proceedings of the 2010 4th International Power Engineering and Optimization Conference, Shah Alam, Malaysia, 23–24 June 2010; pp. 126–131.
9. Lim, D.K.; Cho, Y.S.; Ro, J.S.; Jung, S.Y.; Jung, H.K. Optimal Design of an Axial Flux Permanent Magnet Synchronous Motor for the Electric Bicycle. *IEEE Trans. Magn.* **2016**, *52*, 1–4. [CrossRef]
10. Kim, J.S.; Lee, J.H.; Kim, Y.J.; Jung, S.Y. Characteristics analysis method of axial flux permanent magnet motor based on 2-D finite element analysis. *IEEE Trans. Magn.* **2017**, *53*, 1–4. [CrossRef]
11. Hemeida, A.; Sergeant, P. Analytical Modeling of Surface PMSM Using a Combined Solution of Maxwell–s Equations and Magnetic Equivalent Circuit. *IEEE Trans. Magn.* **2014**, *50*, 1–13. [CrossRef]
12. Xia, C.; Zhao, J.; Yan, Y.; Shi, T. A novel direct torque control of matrix converter-fed PMSM drives using duty cycle control for torque ripple reduction. *IEEE Trans. Ind. Electron.* **2013**, *61*, 2700–2713. [CrossRef]
13. Vafaie, M.H.; Dehkordi, B.M.; Moallem, P.; Kiyoumarsi, A. Minimizing torque and flux ripples and improving dynamic response of PMSM using a voltage vector with optimal parameters. *IEEE Trans. Ind. Electron.* **2015**, *63*, 3876–3888. [CrossRef]
14. Wang, D.; Lin, H.; Yang, H.; Wang, K. Cogging torque optimization of flux memory pole-changing permanent magnet machine. *IEEE Trans. Appl. Supercond.* **2016**, *26*, 1–5. [CrossRef]

15. Lai, C.; Feng, G.; Mukherjee, K.; Kar, N.C. Investigations of the influence of PMSM parameter variations in optimal stator current design for torque ripple minimization. *IEEE Trans. Energy Convers.* **2017**, *32*, 1052–1062. [CrossRef]
16. Wahsh, S.; Shazly, J.; Yassin, A. Steady state heat conduction problems of AFPMSM using 3D Finite Element. In Proceedings of the 18th International Middle-East Power Systems Conference, Helwan Univ, ON, Egypt, 27–29 December 2016; pp. 949–953.
17. Chen, Q.; Liang, D.; Gao, L.; Wang, Q.; Liu, Y. Hierarchical thermal network analysis of axial-flux permanent-magnet synchronous machine for electric motorcycle. *IET Electr. Power Appl.* **2018**, *12*, 859–866. [CrossRef]
18. Rasekh, A.; Sergeant, P.; Vierendeels, J. Fully predictive heat transfer coefficient modeling of an axial flux permanent magnet synchronous machine with geometrical parameters of the magnets. *Appl. Thermal Eng.* **2017**, *110*, 1343–1357. [CrossRef]
19. De Bisschop, J.; Sergeant, P.; Dupré, L. Demagnetization fault detection in axial flux PM machines by using sensing coils and an analytical model. *IEEE Trans. Magn.* **2017**, *53*, 1–4. [CrossRef]
20. De Bisschop, J.; Sergeant, P.; Hemeida, A.; Vansompel, H.; Dupre, L. Analytical Model for Combined Study of Magnet Demagnetization and Eccentricity Defects in Axial Flux Permanent Magnet Synchronous Machines. *IEEE Trans. Magn.* **2017**, *53*, 1–12. [CrossRef]
21. De Bisschop, J.; Abdallh, A.; Sergeant, P.; Dupré, L. Identification of Demagnetization Faults in Axial Flux Permanent Magnet Synchronous Machines Using an Inverse Problem Coupled With an Analytical Model. *IEEE Trans. Magn.* **2014**, *50*, 1–4. [CrossRef]
22. Hemeida, A.; Sergeant, P.; Vansompel, H. Comparison of Methods for Permanent Magnet Eddy-Current Loss Computations With and Without Reaction Field Considerations in Axial Flux PMSM. *IEEE Trans. Magn.* **2015**, *51*, 1–11. [CrossRef]
23. Scheerlinck, B.; De Gersem, H.; Sergeant, P. 3D Eddy-Current and Fringing-Flux Distribution in an Axial-Flux Permanent-Magnet Synchronous Machine with Stator in Laminated Iron or SMC. *IEEE Trans. Magn.* **2015**, *51*, 1–4. [CrossRef]
24. Chen, Q.; Liang, D.; Jia, S.; Ze, Q.; Liu, Y. Loss Analysis and Experiment of Fractional-Slot Concentrated-Winding Axial Flux PMSM for EV Applications. In Proceedings of the 10th IEEE Annual Energy Conversion Congress and Exposition, Portland, ON, USA, 23–27 September 2018; pp. 4329–4335.
25. Fei, W.; Luk, P.C.K. Torque ripple reduction of axial flux permanent magnet synchronous machine with segmented and laminated stator. In Proceedings of the 2009 IEEE Energy Conversion Congress and Exposition, San Jose, CA, USA, September 2009; pp. 132–138.
26. Woolmer, T.; McCulloch, M. Analysis of the yokeless and segmented armature machine. In Proceedings of the 2007 IEEE International Electric Machines & Drives Conference, Antalya, Turkey, 3–5 May 2007; pp. 704–708.
27. Aydin, M.; Huang, S.; Lipo, T. Axial flux permanent magnet disc machine: A review. In Proceedings of the Symposium on Power Electronics, Electrical Drives, Automation, and Motion (SPEEDAM), Capri, Italy, 16–18 June 2004; pp. 61–71.
28. Hosseini, S.M.; Agha-Mirsalim, M.; Mirzaei, M. Design, prototyping, and analysis of a low cost axial-flux coreless permanent-magnet generator. *IEEE Trans. Magn.* **2008**, *44*, 75–80. [CrossRef]